sustainability

MDPI

Article

Optimization of a Biomass-Based Power and Fresh Water-Generation System by Machine Learning Using Thermoeconomic Assessment

Fatemeh Parnian Gharamaleki [1], Shayan Sharafi Laleh [2], Nima Ghasemzadeh [2,*], Saeed Soltani [3,*] and Marc A. Rosen [4]

[1] Faculty of Chemical and Petroleum Engineering, University of Tabriz, Tabriz 16471, Iran; fatemeh.parniangh@gmail.com
[2] Faculty of Mechanical Engineering, University of Tabriz, Tabriz 16471, Iran; shayan.sharafi99@ms.tabrizu.ac.ir
[3] Faculty of Engineering and Natural Sciences, Antalya Bilim University, 07190 Antalya, Turkey
[4] Faculty of Engineering and Applied Science, University of Ontario Institute of Technology, 2000 Simcoe Street North, Oshawa, ON L1G 0C5, Canada
* Correspondence:nimaghasemzadeh98@ms.tabrizu.ac.ir (N.G.); soltani929@gmail.com or saeed.soltani@antalya.edu.tr (S.S.); Tel.: +98-921-049-8716 (N.G.); +90-242-245-00-00 (S.S.)

Abstract: Biomass is a viable and accessible source of energy that can help address the problem of energy shortages in rural and remote areas. Another important issue for societies today is the lack of clean water, especially in places with high populations and low rainfall. To address both of these concerns, a sustainable biomass-fueled power cycle integrated with a double-stage reverse osmosis water-desalination unit has been designed. The double-stage reverse osmosis system is provided by the 20% of generated power from the bottoming cycles and this allocation can be altered based on the needs for freshwater or power. This system is assessed from energy, exergy, thermoeconomic, and environmental perspectives, and two distinct multi-objective optimization scenarios are applied featuring various objective functions. The considered parameters for this assessment are gas turbine inlet temperature, compressor's pressure ratio, and cold end temperature differences in heat exchangers 2 and 3. In the first optimization scenario, considering the pollution index, the total unit cost of exergy products, and exergy efficiency as objective functions, the optimal values are, respectively, identified as 0.7644 kg/kWh, 32.7 USD/GJ, and 44%. Conversely, in the second optimization scenario, featuring the emission index, total unit cost of exergy products, and output net power as objective functions, the optimal values are 0.7684 kg/kWh, 27.82 USD/GJ, and 2615.9 kW.

Keywords: biomass gasification; reverse osmosis; thermoeconomic; grey wolf optimization

Citation: Parnian Gharamaleki, F.; Sharafi Laleh, S.; Ghasemzadeh, N.; Soltani, S.; Rosen, M.A. Optimization of a Biomass-Based Power and Fresh Water-Generation System by Machine Learning Using Thermoeconomic Assessment. *Sustainability* **2024**, *16*, 8956. https://doi.org/10.3390/su16208956

Academic Editor: Maurizio Volpe

Received: 4 September 2024
Revised: 9 October 2024
Accepted: 14 October 2024
Published: 16 October 2024

1. Introduction

There are now two main tendencies in terms of environmental and economic challenges. First, the Intergovernmental Panel on Climate Change (IPCC) states that significant adjustments to energy, land, urban infrastructure, and industrial systems are required to keep global heating to 1.5 °C with minimal overshoot [1,2]. Increasing public understanding of the factors that contribute to environmental deterioration is important for accelerating the global switch to low-carbon energy sources and achieving sustainable development [3].

The progressive expansion of domestic renewable energy sources (RESs), enhancement of energy efficiency, and reduction of import dependence on fossil fuels are some of the primary objectives of the EU energy strategy [4]. The optimal scheduling and integration of renewable energy sources and effective energy management face numerous obstacles. The integration and optimization of power generation are more challenging due to the unpredictable and uncertain character of RES, particularly wind and solar energy. Unlike

solar and wind energy, biomass is a more dependable and controllable source of energy. Biomass is comprised of a wide range of materials such as agricultural waste, wood, municipal waste, algae, etc., and the abundance of these materials is an opportunity for a valuable energy source. The public's increased acceptance of these technologies is a key component in using various RESs [5,6]. RESs increase the majority of the population's access to energy, and reduce local and global pollutant emissions and increase the potential for local socio-economic development. Additionally, electricity produced from renewable resources significantly lowers greenhouse gas emissions and energy poverty [7–9]. Co-firing biomass and fossil wastes for energy production is still a viable option for the efficient use of industrial and agricultural waste. An important factor in the rise in global energy consumption is bioenergy. It is also the fourth-largest energy source in the world and likely to be an essential part of the renewable energy mix because of its green, low-carbon, and clean characteristics as well as its significant development potential [10–12].

The clean conversion of diverse types of solid biomass to gas by biomass gasification has the potential to become an important process. For a variety of uses, biomass has the potential to be converted into several types of biofuel and biochemical. Gasifiers are one of the more practical options for converting biomass into valuable energy commodities. There are various gasification agents like air, steam, and oxygen and differing temperatures and pressures have considerable effects on gasification processes. There are many different methods to do this. Updraft and downdraft are two of the configurations for fixed bed gasifiers, and the downdraft fluidized bed configuration generates syngas of higher heating value [13–15].

The lack of clean water is another significant problem nowadays, particularly in warmer and more crowded locations. Large-scale renewable energy-assisted desalination systems still have higher clean water-production costs than conventional fossil fuel-based systems. Energy and material resources are needed to create and operate water-purifying systems. The most effective desalination method, which may be combined with various RESs, is reverse osmosis (RO). Reverse osmosis technology is currently the best technology for treating sewage. A RO water filter system can be suitable for campus water, canteen water, drinking water, food-processing water, chemical-production water, experimental water, aquaculture water, industrial water, hotel water, bathing water, and other applications and industries. Advanced RO systems can be developed, and their designs can be made advantageous with accurate mathematical modeling of the RO system. Given that intermittent RESs can shorten the lifespan of RO membranes and other components, RES optimization is needed to meet the RO demand [16–19]. There are numerous power-generation cycles and configurations to provide the necessary power for RO units. One of the well known power cycles that can use biomass as fuel is the gas turbine (GT). GTs operate at high temperatures and, because of this, they are often combined with various power-production processes for heat recovery, such as closed Brayton cycles, Rankine cycles, and fuel cells [20,21].

Biomass is a viable and accessible energy source that can help address the problem of energy shortages in rural and remote areas. Another important issue for societies today is the lack of clean water, especially in places with high populations and low rainfall. The objective of this paper is to address both of these concerns by developing a sustainable biomass-fueled power cycle integrated with double-stage reverse osmosis water desalination.

2. Previous Works

Much research has been reported on the topics central to the present study, and key studies are described here.

2.1. Biomass-Based Power Generation

An effective technique that uses solar power as a heat carrier for biomass gasification is the combination of biomass and solar photothermal gasification. However, the effects of biomass ash can erode the heat carrier that delivers heat to the biomass feedstock, and the

erosion problem worsens as the number of cycles rises. Li et al. [22] looked into the erosion and adhesion brought on by maize stalk ash (CSA) repeatedly sintering to heat carrier particles (Al_2O_3). The primary components in CSA that erode Al_2O_3 particles are K and Si, and the more sintering cycles there are, the deeper the erosion of these elements. Using thermodynamic laws, Yilmaz et al. [23] conducted a thorough thermodynamic assessment of an integrated plant using biomass in their work. Biogas generated from demolition wood biomass powers the multi-generation plant type. The plant's primary components are a Rankine cycle, hydrogen production, compression of hydrogen, clean water-production system, biomass gasifier cycle, and gas turbine sub-plant. This facility produces clean water, power, hydrogen, and warmth. The findings show that the planned plant's overall energy and energy efficiencies are 52.84% and 46.59%, respectively. Additionally, the biomass gasification unit has the greatest irreversibility rate of 12,685 kW, and the total irreversibility rate of the proposed cycle is 37,743 kW. To increase biomass utilization, Chen et al. [24] integrated supercritical CO_2 power cycles, biomass gasification-based power generation, and coal-fired power production. The clean syngas produced by biomass gasification is utilized by a GT, and the hot exhaust that is produced is then used to heat the feedwater streams of the coal power plant and the CO_2 stream of the sCO_2 (supercritical carbon dioxide) cycle. The performance of the proposed scheme, based on a 2.22 kg/s biomass consumption rate and a 350 MW coal power plant, was investigated using thermodynamic and economic analyses. The findings showed that, when coal-generated net power remains constant, biomass-to-electricity achieves energy and exergy efficiencies of about 44% and 41%, respectively, at the design point. Roy et al. [25] proposed a novel externally fired GT, molten carbonate fuel cell, biomass gasifier, and water-heating facility that has been coupled to form a combined heat and power system, and performed thermodynamic and economic analyses. According to the optimization, the cogeneration system has the highest energy efficiency (41.2%) and the lowest levelized energy cost (0.044 USD/kWh).

2.2. Reverse Osmosis Desalination Unit

Using actual plant-operation data, Blanco-Marigorta et al. [26] performed an exergo-environmental analysis of a reverse osmosis desalination facility in the Canary Islands. The plant can produce 82,000 m^3/day in theory. Depending on the energy recovery, the phases of reverse osmosis, the filtration technology, and the pressurization of the feed water, several combinations are conceivable. The high-pressure pump and the first-stage reverse osmosis membrane module are responsible for most of the exergy destruction. Abbasi et al. [27] examined the application of high-temperature thermal energy storage to create electricity, cooling, and fresh water, and assessed three different modes of a novel integrated system. The RO desalination unit produces fresh water while the absorption refrigeration cycle provides cooling. The proposed system's energy efficiency is calculated to be 14.4% at most, while its energy efficiency is 40.5% with a total product cost rate of 30.5 USD/GJ. Nemati et al. [28] proposed a cogeneration system based on a series of two-stage organic Rankine cycles (ST_{ORC}) using a zeotropic mixture as the working fluid integrated with a reverse osmosis desalination (RO) unit for waste heat recovery from a heavy-duty marine diesel engine. The proposed system is thermodynamically simulated and assessed thorough energy, exergy, and exergoeconomics analyses. The optimization results show that the values of the objective functions are increased by 37.0% and 59.1 USD/GJ, respectively, at the final Pareto frontier optimal design point. Abdolalipouradl et al. [29] presented two unique trigeneration systems based on single and double flash methods that produce power, hydrogen, and fresh water using geothermal energy, and carried out thermodynamic and exergoeconomic analyses. Both cycles employ reverse osmosis desalination, an organic Rankine cycle, and a proton-exchange membrane electrolyzer to produce hydrogen and fresh water. The results demonstrate that the double-flash trigeneration system (system 2) performs better from exergy and exergoeconomic viewpoints than the single flash-based one (system 1), leading to the achievement of the system's optimum values for net power output, hydrogen production rate, desalinated water rate, and energy and

exergy efficiencies. Pan et al. [30] investigated the performance of four different CO_2 Brayton-based dual-loop cycles to harness waste heat from a dual combustion engine. They achieved a notable 7% enhancement in energy efficiency when integrating a carbon dioxide Brayton cycle with an organic Rankine cycle, compared to scenarios lacking waste heat recovery. In a separate study, Song et al. [31] proposed four configurations combining carbon dioxide Brayton and organic Rankine cycles utilizing geothermal water in Spain. These configurations exhibited a substantial increase in total electricity generation ranging from 22% to 45% when contrasted with the conventional supercritical carbon dioxide cycle. Furthermore, other researchers [32] examined the amalgamation of a supercritical carbon dioxide cycle and an organic Rankine cycle as a downstream cycle for fresh water production via reverse osmosis desalination, utilizing exhaust gases from a gas turbine. The utilization of supercritical carbon dioxide and organic Rankine cycles for waste heat recovery from the gas turbine resulted in a respective increase in overall efficiency by 10.9% and 2%. Additionally, Wang et al. [33] undertook an analysis and optimization of a trigeneration system comprised of an organic Rankine cycle, a supercritical carbon dioxide cycle, a gas turbine, and an absorption refrigeration system.

2.3. Merits of the Present Study

This proposed system in the present study is a cogeneration externally fired GT integrated with an intercooler sCO_2 Brayton cycle and a regenerative organic Rankine cycle (ORC) fueled solely by biomass, coupled with a double-stage RO unit with a Pelton turbine (PT) for fresh water production. The use of biomass leads to significantly lower flue gas emissions because of its accessibility and ease of substitution compared to fossil fuels. This system shows generally how efficient and economically viable it is to use a biomass-based cycle for power and fresh water production. The considered biomass for this system is wood which is one of the most common and easy-to-access sources of biomass. This system is environment-benign due to its products and methods of power generation. Another positive aspect of this system is that it can be utilized in remote locations and places where clean water is not accessible. The benefit of using double-stage RO is that the higher amounts of water can be into drawn the unit and desalinated. Rejected brine from the RO unit has a substantial amount of pressure; to benefit from this, a PT is utilized to increase the outlet water of the system. A comprehensive study is conducted to evaluate the system's viability from energy, exergy, exergoeconomic, and environmental points of view. To have a better perspective on the present system and to find the optimal value for key parameters of the system, two separate multi-objective optimization situations with various parameters are employed. The novelty of the investigation is in the new configuration of the system which is composed of three different types of power-generation cycles and an RO unit and its analysis. The study of this cycle is also comprehensive and covers all the aspect of a power and water dual generation system.

3. System Description and Assumptions

3.1. System Description

The system proposed here is comprised of four sub-cycles, three of which are power-generation layouts, while the last is a water desalination RO unit. The gas Brayton cycle is considered the main cycle and the other bottoming cycles function using its products. Biomass (wood) is turned into the syngas in the gasifier and is burned in the combustion chamber to run the system. A detailed description of biomass and gasifier parameters has been presented elsewhere [21]. After heating the compressed air in the heat exchanger (HE) no. 1, product gases also heat the CO_2 using HE_2 in the intercooling Brayton cycle as well as R123 with HE_3 in the ORC for high heat recovery. A portion of the generated power from the bottoming cycles is allocated to the multiple pumps in the double-stage RO unit. Additionally, generated power in the Pelton turbine is also utilized in the RO unit. Initially, water is drawn into the unit by the feed pump (FPu) and its pressure is raised to the required level (which is 6.23 MPa in this case for the reactions that take place) by the

second stage of compression in the high-pressure pump (HPPu). At this step, high-pressure water goes through multiple layers of desalination filters at stage 1, and the rejected brine is then pressurized to the required pressure by the boost pump (BPu). After the second stage of desalination, the brine is expanded to the environmental pressure in the Pelton turbine which has the advantages of simple construction, easy maintenance, and high overall efficiency. Figure 1 illustrates the overall proposed system.

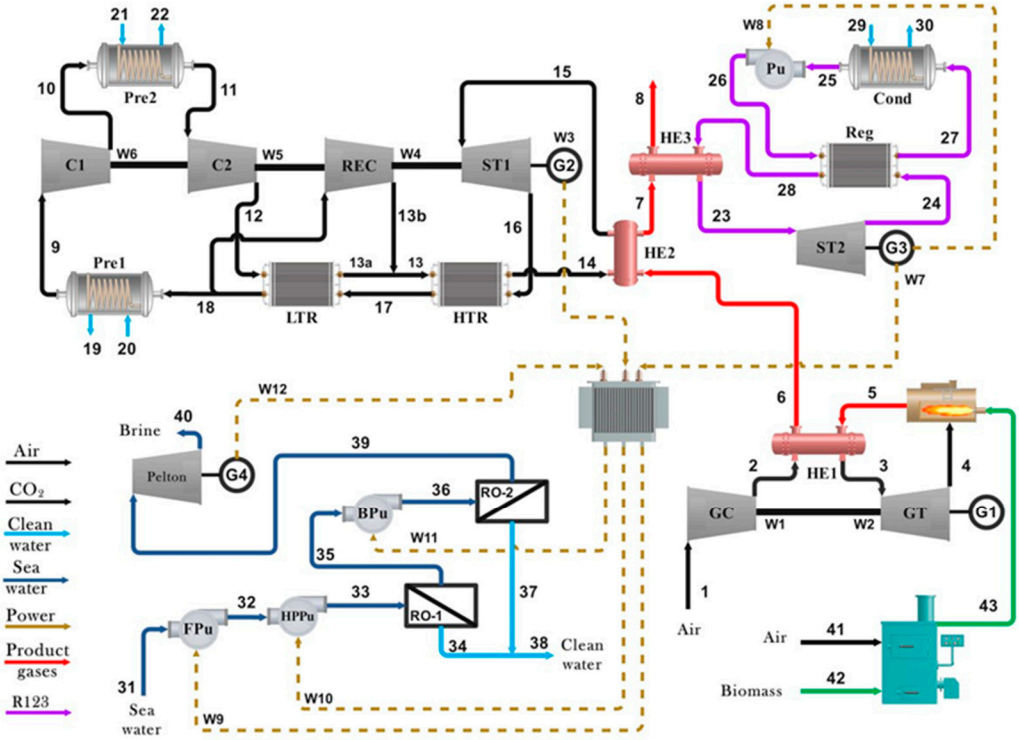

Figure 1. Schematic of the proposed system.

3.2. Assumptions and Key Parameters

Several assumptions are considered for the system's thermodynamic simulation:

- The system performs at steady state.
- Ambient temperature and pressure are considered to be 298 K and 101.3 kPa, respectively.
- Heat losses at heat exchangers, condensers, and recuperators can be neglected.
- R123 leaves the condenser as a saturated liquid.

Table 1 lists data for the important and key parameters of the system.

Table 1. Key system parameters and their values [29,34].

Parameter	Value
Gas turbine	
GTIT	1400 K
T_g	1073 K
T_6	800 K
AC r_p	10
$\eta_{is,AC}$	0.87
$\eta_{is,GT}$	0.89

Table 1. *Cont.*

sCO_2 cycle	
T_{15}	700 K
T_{19}, T_{21}, and T_{29}	298 K
P_{10}	11,000 kPa
Maximum CO_2 pressure at Brayton cycle	2000 kPa
Minimum CO_2 pressure at Brayton cycle	7400 kPa
$\varepsilon_{HTR\ \&\ LTR}$	0.86
$\eta_{is,\ C1,C2,REC}$	0.89
$\eta_{is,T,CO2}$	0.9
ORC cycle	
T_{23}	500 K
Maximum R123 pressure	5000 kPa
Minimum R123 pressure	101.3 kPa
$\eta_{is,ST}$	0.9
$\eta_{is,Pump}$	0.8
ε_{Reg}	0.86
RO unit	
T_{water} in RO unit	298 K
$\eta_{is,FPu,HPPu,BPu}$	0.767
$\eta_{is,Pelton}$	0.79

4. System Modeling

4.1. Thermodynamic Modeling and Analysis

In this section, the system with its components is thermodynamically assessed and characterized, in part for the purpose of conducting an exergoeconomic analysis subsequently. When modeling the existing system, we consider the potential and kinetic energy of each stream and the pressure drop across the entire system to be insignificant and the system to operate under steady-state conditions. The assessment utilizes rate balances for mass, energy, and exergy, which follow:

$$\sum \dot{m}_{in} - \sum \dot{m}_{out} = 0 \tag{1}$$

$$\dot{Q} - \dot{W} = \sum (\dot{m}h)_{in} - \sum (\dot{m}h)_{out} \tag{2}$$

$$\dot{E}x_{heat} - \dot{W} = \sum (\dot{m}ex)_{in} - \sum (\dot{m}ex)_{out} + \dot{E}x_{dest} \tag{3}$$

In the current work, a downdraft gasifier which has four zones—drying, pyrolysis, reduction, and combustion—is considered.

4.1.1. Gasifier

According to the equilibrium model, all gasifier reactions should be in thermodynamic equilibrium. Before exiting the gasifier, the pyrolysis products are supposed to burn and reach equilibrium in the reduction zone. The reactions that take place during gasification are:

$$C + CO_2 \leftrightarrow 2CO \tag{4}$$

$$C + H_2O \leftrightarrow CO + H_2 \tag{5}$$

$$C + 2H_2 \leftrightarrow CH_4 \tag{6}$$

$$CO + H_2O \leftrightarrow CO_2 + H_2 \quad (7)$$

Based on Zainal et al. [35], the overall gasification reaction for the downdraft gasifiers is written as:

$$C_XH_YO_Z + w\ H_2O + m(O_2 + 3.76N_2) \rightarrow n_1H_2 + n_2CO + n_3CO_2 + n_4H_2O + n_5CH_4 + n_6N_2 \quad (8)$$

In Equation (8), w and m represent the values of water and oxygen per kmol of biomass, respectively. The biomass is mainly composed of carbon, hydrogen, and oxygen, while the municipal waste also contains a small fraction of nitrogen. Zainal et al. [35] assume that municipal waste has a composition of $CH_{1.502}O_{0.5189}N_{0.02162}$ and a higher heating value (HHV) of 433,034 kJ/kmol. Soltani et al. [34] consider a complete combustion reaction in the CC by the mixture of syngas and air from GT1, which can be expressed as:

$$\begin{gathered} n_1H_2 + n_2CO + n_3CO_2 + n_4H_2O + n_5CH_4 + n_6N_2 + n_{Air}(O_2 + 3.76N_2) \\ \rightarrow n_7CO_2 + n_8H_2O + n_8H_2O + n_9O_2 + (n_6 + 3.76n_{Air})N_2 \end{gathered} \quad (9)$$

Soltani et al. [34] define the equilibrium constant for the methane formation as:

$$K_1 = \frac{P_{CH_4}}{\left(P_{H_2}\right)^2} \quad (10)$$

and the shift reaction as (Soltani et al. [34]):

$$K_2 = \frac{P_{CO_2}P_{H_2}}{P_{CO}P_{H2O}} \quad (11)$$

By using the syngas coefficient values, we can calculate the equilibrium constant values for the methane generation and water–gas shift reactions. Soltani et al. [34] give the equilibrium constants for these reactions via Equations (10) and (11), respectively:

$$K_1 = \frac{n_5}{(n_1)^2} \quad (12)$$

and

$$K_2 = \frac{n_3n_1}{n_2n_4} \quad (13)$$

Soltani et al. [34] and Zainal et al. [35] provide other relevant equations such as equilibrium constants for simulating the gasification process.

4.1.2. Reverse Osmosis Unit

The RO module transforms seawater into fresh water by elevating its pressure in both the FPu and High-Pressure Pump (HPPu). Additionally, a portion of the required energy for the BPu is supplied by a Pelton turbine. This energy is utilized to boost the pressure of the discharged saline water from RO-1, enabling a repeat of the desalination process with RO-2. The following three equations are employed to establish the salinity levels of the brine and fresh water:

$$(\dot{m}y_s)_{33} = (\dot{m}y)_{34} + (\dot{m}y_s)_{35} \quad (14)$$

$$(\dot{m}y_s)_{36} = (\dot{m}y)_{37} + (\dot{m}y_s)_{39} \quad (15)$$

$$(\dot{m}y_s)_{38} = (\dot{m}y)_{38} + (\dot{m}y_s)_{34} \quad (16)$$

Here, y and y_s are the clean water mass fraction and salt water mass fraction, respectively.

4.1.3. ORC Cycle

The ORC constitutes a pivotal element in the system modeling, serving as an efficient thermodynamic process for power generation. In the ORC, a working fluid (R123) with a

lower boiling point than that of water is employed to transfer heat from a heat reservoir to the working fluid which has the advantage of waste heat recovery at heavy load. This heat causes the fluid to vaporize, driving a turbine and subsequently generating power. The mathematical representation of the Organic Rankine Cycle (ORC) involves several equations that capture the energy balance, heat transfer processes, and overall performance. Below are the fundamental equations describing the key components of the ORC cycle:

Energy rate balance for the condenser:

$$\dot{Q}_{Cond} = \dot{m}_{27}(h_{27} - h_{25}), \dot{Q}_{Cond} = \dot{m}_{29}(h_{30} - h_{29}) \quad (17)$$

Energy rate balance for the turbine:

$$\dot{W}_{ST} = \dot{m}_{23}(h_{23} - h_{24}) \quad (18)$$

Net work output rate:

$$\dot{W}_{net} = \dot{W}_{turbine} - \dot{W}_{Pump} \quad (19)$$

where

$$\dot{W}_{Pump} = \dot{m}_{25}(h_{26} - h_{25}) \quad (20)$$

The efficiency of the ORC can be written as:

$$\eta_{ORC} = \frac{\dot{W}_{net}}{\dot{Q}_{in}} \quad (21)$$

4.1.4. sCO_2 Cycle

The expansion and compression processes in the sCO_2 cycle are important components influencing the overall efficiency. CO_2 is chemically inert and nontoxic and is non-flammable. Detailed modeling of the turbine and compressor involves accounting for isentropic efficiencies, pressure ratios, and temperature changes. The turbine, where the sCO_2 expands, and the compressor, where it is compressed, play significant roles in determining the net work output of the cycle. Relevant energy rate balances for these devices, specifically C_1, C_2, REC, and ST_1, respectively, follow:

$$\dot{W}_{C1} = \dot{m}_9(h_{10} - h_9) \quad (22)$$

$$\dot{W}_{C2} = \dot{m}_{11}(h_{12} - h_{11}) \quad (23)$$

$$\dot{W}_{REC} = \dot{m}_{18}(h_{13b} - h_{18}) \quad (24)$$

$$\dot{W}_{ST1} = \dot{m}_{15}(h_{15} - h_{16}) \quad (25)$$

The effectiveness of heat exchange significantly impacts the overall cycle efficiency, making it necessary to analyze the performances of recuperators, precoolers, and reheaters. Energy balances for devices HRT, LTR, Pre1, and Pre2 are as follows:

$$h_{16} - h_{17} = h_{14} - h_{13} \quad (26)$$

$$h_{17} - h_{18} = h_{13} - h_{12} \quad (27)$$

$$\dot{Q}_{Pre1} = \dot{m}_{18}(h_9 - h_{18}), \dot{Q}_{Pre1} = \dot{m}_{20}(h_{20} - h_{19}) \quad (28)$$

$$\dot{Q}_{Pre2} = \dot{m}_{10}(h_{11} - h_{10}), \dot{Q}_{Pre2} = \dot{m}_{21}(h_{21} - h_{22}) \quad (29)$$

Equations for the energy analysis of the system are listed in Table 2.

Table 2. Governing energy equations of the system.

Component	Energy Balance Equation
Gas turbine	
GC	$\dot{W}_{GC} = \dot{m}_1(h_2 - h_1)$
GT	$\dot{W}_{GT} = \dot{m}_3(h_3 - h_4)$
HE1	$\dot{H}_2 + \dot{H}_5 = \dot{H}_3 + \dot{H}_6$
CC	$\left(-0.02\overline{\lambda}LHV + h_{air} + \overline{\lambda h}_{fuel} - (1+\overline{\lambda})h_{prod} = 0\right.$
RO	
FPu	$\dot{W}_{Fpu} = \frac{\dot{V}_{31}\cdot\Delta P}{\mu_{Fpu}}$
HPPu	$\dot{W}_{HPpu} = \frac{\dot{V}_{32}\cdot\Delta P}{\mu_{HPpu}}$
BPu	$\dot{W}_{Bpu} = \frac{\dot{V}_{35}\cdot\Delta P}{\mu_{Bpu}}$
PT	$\dot{W}_{PT} = \dot{m}_{39}(h_{39} - h_{40})$
RO-1	-
RO-2	-
R123 cycle	
Pu	$\dot{W}_{Pump} = \dot{m}_{25}(h_{26} - h_{25})$
Cond	$\dot{Q}_{Cond} = \dot{m}_{27}(h_{27} - h_{25}), \dot{Q}_{Cond} = \dot{m}_{29}(h_{30} - h_{29})$
Reg	$\dot{H}_{24} + \dot{H}_{26} = \dot{H}_{27} + \dot{H}_{28}$
ST2	$\dot{W}_{ST} = \dot{m}_{23}(h_{23} - h_{24})$
HE3	$\dot{H}_{28} + \dot{H}_7 = \dot{H}_{23} + \dot{H}_8$
sCO_2 cycle	
HTR	$h_{16} - h_{17} = h_{14} - h_{13}$
LTR	$(1-x)h_{13} - h_{12} = h_{17} - h_{18}$
Pre1	$\dot{Q}_{Pre1} = \dot{m}_{18}(h_9 - h_{18}), \dot{Q}_{Pre1} = \dot{m}_{20}(h_{20} - h_{19})$
Pre2	$\dot{Q}_{Pre2} = \dot{m}_{10}(h_{11} - h_{10}), \dot{Q}_{Pre2} = \dot{m}_{21}(h_{21} - h_{22})$
C1	$\dot{W}_{C1} = \dot{m}_9(h_{10} - h_9)$
C2	$\dot{W}_{C2} = \dot{m}_{11}(h_{12} - h_{11})$
REC	$\dot{W}_{REC} = \dot{m}_{18}(h_{13b} - h_{18})$
ST1	$\dot{W}_{ST1} = \dot{m}_{15}(h_{15} - h_{16})$

4.1.5. Exergy Equations

Exergy analysis merges the principles of the second law of thermodynamics with equations governing mass and energy balances. A general exergy rate balance follows:

$$\dot{E}x_{di} = \sum\left(1 - \frac{T_o}{T}\right)\dot{Q}_i - \dot{W}_i + \sum\dot{E}x_{in} - \sum\dot{E}x_{out} \quad (30)$$

Here, $\sum Ex$ represents the rate of exergy associated flows (inflow or outflow) for the component, and $\dot{E}x_{di}$ denotes the exergy destruction rate in device i. This equation underscores the significance of the dead state temperature (T_o) and the boundary temperature (T) in determining the rates of exergy destruction, or available energy dissipation, within the device. While certain constituents, such as air, exhibit zero or little chemical exergy

due to their compositions relative to the reference environment, RO cycles, which involve variable compositions, necessitate specific mathematical expressions (refer to Table 3). For the system, the ratio of individual exergy destruction of component k to the overall exergy destruction can be expressed as

$$Y_k^* = \frac{\dot{E}x_{D,k}}{\dot{E}x_{D,total}} \tag{31}$$

Table 3. Governing exergy equations of the system.

Component	Exergy Balance Equation
Gas turbine	
GC	$\dot{E}_1 + \dot{W}_{GC} = \dot{E}_2 + \dot{E}_{D,GC}$
GT	$\dot{E}_3 + \dot{W}_{GT} = \dot{E}_4 + \dot{E}_{D,GT}$
HE1	$\dot{E}_2 + \dot{E}_5 = \dot{E}_3 + \dot{E}_6 + \dot{E}_{D,HE1}$
CC	$\dot{E}_{43} + \dot{E}_4 = \dot{E}_5 + \dot{E}_{D,CC}$
RO	
FPu	$\dot{E}_{31} + \dot{W}_{Fpu} = \dot{E}_{32} + \dot{E}_{D,Fpu}$
HPPu	$\dot{E}_{32} + \dot{W}_{HPpu} = \dot{E}_{33} + \dot{E}_{D,HPpu}$
BPu	$\dot{E}_{35} + \dot{W}_{Bpu} = \dot{E}_{36} + \dot{E}_{D,Bpu}$
PT	$\dot{E}_{39} = \dot{E}_{40} + \dot{W}_{PT} + \dot{E}_{D,PT}$
RO-1	$\dot{E}_{33} = \dot{E}_{34} + \dot{E}_{35} + \dot{E}_{D,RO-1}$
RO-2	$\dot{E}_{36} = \dot{E}_{37} + \dot{E}_{39} + \dot{E}_{D,RO-2}$
R123 cycle	
Pump	$\dot{E}_{25} + \dot{W}_{Pump} = \dot{E}_{26} + \dot{E}_{D,Pu}$
Cond	$\dot{E}_{27} + \dot{E}_{29} = \dot{E}_{25} + \dot{E}_{30} + \dot{E}_{D,Cond}$
Reg	$\dot{E}_{24} + \dot{E}_{26} = \dot{E}_{27} + \dot{E}_{28} + \dot{E}_{D,HE3}$
ST2	$\dot{E}_{23} = \dot{E}_{24} + \dot{W}_{ST2} + \dot{E}_{D,ST2}$
HE3	$\dot{E}_{28} + \dot{E}_7 = \dot{E}_{23} + \dot{E}_8 + \dot{E}_{D,HE3}$
sCO_2 cycle	
HTR	$\dot{E}_{16} + \dot{E}_{13} = \dot{E}_{14} + \dot{E}_{17} + \dot{E}_{D,HTR}$
LTR	$\dot{E}_{13} + \dot{E}_{18} = \dot{E}_{17} + \dot{E}_{12} + \dot{E}_{D,LTR}$
Pre1	$\dot{E}_{18} + \dot{E}_{20} = \dot{E}_9 + \dot{E}_{19} + \dot{E}_{D,Pre1}$
Pre2	$\dot{E}_{10} + \dot{E}_{21} = \dot{E}_{11} + \dot{E}_{22} + \dot{E}_{D,Pre2}$
C1	$\dot{E}_9 + \dot{W}_{C1} = \dot{E}_{10} + \dot{E}_{D,C1}$
C2	$\dot{E}_{11} + \dot{W}_{C2} = \dot{E}_{12} + \dot{E}_{D,C2}$
REC	$\dot{E}_{18} + \dot{W}_{REC} = \dot{E}_{13b} + \dot{E}_{D,REC}$
ST1	$\dot{E}_{23} = \dot{E}_{24} + \dot{W}_{ST2} + \dot{E}_{D,ST2}$

4.1.6. Exergoeconomic Equations

This section delves into the amalgamation of exergetic and economic principles for system assessment, which gives rise to exergoeconomic concepts with the goal of minimizing both total cost and exergy destruction [36]. First, the evaluation includes presenting the cost equilibrium for the kth component using Equation (32), which asserts that the cost rate

of input exergy combined with the investment cost rate of a component equals the cost rate of output exergy. Employing the average cost per unit of exergy (c), which is needed to analyze the system's products, the method determines each stream's cost rate ($\dot{C}$). That is,

$$\dot{C}_{q,k} + \sum \dot{C}_{i,k} + \dot{Z}_k = \dot{C}_{w,k} + \sum \dot{C}_{e,k} \quad (32)$$

where

$$\dot{C} = c \times \dot{E}x \quad (33)$$

Here, $\dot{Z}_k$ is the sum of capital investments and maintenance cost rates as follows [36]:

$$\dot{Z}_k = \dot{Z}_k^{CI} + \dot{Z}_k^{OM} = \varnothing_r \times \left(\frac{CRF}{N \times 3600}\right) Z_k \quad (34)$$

where CRF denotes the capital recovery factor, $\varnothing_r$ denotes the operation and maintenance factor, and Z_k corresponds to the purchased equipment cost associated with the kth component. The CRF is dependent on the anticipated life cycle (n) and the interest rate (i), as follows [36]:

$$CRF = \frac{i(1+i)^n}{(1+i)^n - 1} \quad (35)$$

Note that the costs of the components need to be standardized, adjusting them from the reference year to the analysis year (2023 here) as follows [36]:

$$Present\ cost = cost\ for\ original\ year \times \frac{cost\ index\ for\ analysis\ year}{cost\ index\ for\ reference\ year} \quad (36)$$

Moreover, the exergoeconomic factor (f_k) is applied to assess the components. The exergoeconomic factor indicates the proportional importance of non-exergy-related costs ($\dot{Z}_k$) and costs linked to exergy destruction and exergy loss ($\dot{D}_{D,k} + \dot{C}_{L,\,k}$) for each individual component [36]:

$$f_k = \frac{\dot{Z}_k}{\dot{Z}_k + \dot{D}_{D,k} + \dot{C}_{L,k}} \quad (37)$$

The relative cost difference (r_k), which represents the deviation of product cost and fuel cost relative to fuel cost, can be written as

$$r_k = \frac{c_{p,k} - c_{F,k}}{c_{F,k}} \quad (38)$$

Details regarding the necessary cost balance and auxiliary equations for all components of the system are given in Tables 4 and 5 [36].

Table 4. Exergoeconomic equations for components of the system.

Component	Cost Balance Equation	Auxiliary Equation
Gas turbine		
(GC)	$\dot{C}_1 + \dot{Z}_{AC} = \dot{C}_2 + \dot{C}_{w,AC}$	-
(GT)	$\dot{C}_3 + \dot{Z}_{GT} = \dot{C}_4 + \dot{C}_{w,GT}$	$c_3 = c_4$
(HE1)	$\dot{C}_2 + \dot{C}_5 + \dot{Z}_{HE1} = \dot{C}_3 + \dot{C}_6$	$c_5 = c_6$
(CC)	$\dot{C}_{42} + \dot{C}_{fuel} + \dot{Z}_{CC} = \dot{C}_{43}$	$\dot{C}_{fuel} = 2$ USD/GJ
RO		
(FPu)	$\dot{C}_{31} + \dot{C}_{w,FPu} + \dot{Z}_{FPu} = \dot{C}_{32}$	-
(HPPu)	$\dot{C}_{32} + \dot{C}_{w,HPPu} + \dot{Z}_{HPPu} = \dot{C}_{33}$	-

Table 4. *Cont.*

Component	Cost Balance Equation	Auxiliary Equation
(BPu)	$\dot{C}_{35} + \dot{C}_{w,BPu} + \dot{Z}_{BPu} = \dot{C}_{36}$	-
(PT)	$\dot{C}_{39} + \dot{Z}_{PT} = \dot{C}_{40} + \dot{C}_{w,PT}$	$c_{39} = c_{40}$
(RO-1)	$\dot{C}_{33} + \dot{Z}_{RO\_1} = \dot{C}_{34} + \dot{C}_{35}$	$c_{34} = c_{35}$
(RO-2)	$\dot{C}_{36} + \dot{Z}_{RO\_2} = \dot{C}_{37} + \dot{C}_{39}$	$c_{37} = c_{39}$
R123 cycle		
(Pump)	$\dot{C}_{25} + \dot{C}_{w,Pump} + \dot{Z}_{Pu} = \dot{C}_{26}$	-
(Cond)	$\dot{C}_{27} + \dot{C}_{29} + \dot{Z}_{Cond} = \dot{C}_{25} + \dot{C}_{30}$	-
(Reg)	$\dot{C}_{24} + \dot{C}_{26} + \dot{Z}_{Reg} = \dot{C}_{27} + \dot{C}_{28}$	-
(ST2)	$\dot{C}_{23} + \dot{Z}_{ST2} = \dot{C}_{24} + \dot{C}_{w,ST2}$	$c_{23} = c_{24}$
(HE3)	$\dot{C}_{28} + \dot{C}_{7} + \dot{Z}_{HE3} = \dot{C}_{23} + \dot{C}_{8}$	$c_{7} = c_{8}$
sCO_2 cycle		
HTR	$\dot{C}_{16} + \dot{C}_{13} + \dot{Z}_{HTR} = \dot{C}_{14} + \dot{C}_{17}$	$c_{16} = c_{17}$
LTR	$\dot{C}_{13} + \dot{C}_{18} + \dot{Z}_{LTR} = \dot{C}_{17} + \dot{C}_{12}$	$c_{18} = c_{17}$
(Pre1)	$\dot{C}_{18} + \dot{C}_{20} + \dot{Z}_{Pre1} = \dot{C}_{9} + \dot{C}_{19}$	$c_{9} = c_{18}$
(Pre2)	$\dot{C}_{10} + \dot{C}_{21} + \dot{Z}_{Pre2} = \dot{C}_{11} + \dot{C}_{22}$	$c_{10} = c_{11} = c_{21}$
(C1)	$\dot{C}_{9} + \dot{C}_{w,C1} + \dot{Z}_{C1} = \dot{C}_{10}$	-
(C2)	$\dot{C}_{11} + \dot{C}_{w,C2} + \dot{Z}_{C2} = \dot{C}_{12}$	-
REC	$\dot{C}_{18} + \dot{Z}_{REC} = \dot{C}_{13b} + \dot{C}_{w,REC}$	$c_{18} = c_{13b}$
(ST1)	$\dot{C}_{15} + \dot{Z}_{ST1} = \dot{C}_{16} + \dot{C}_{w,ST1}$	$c_{16} = c_{5}$

Table 5. Expressions for purchase costs of devices used in the system [37].

Device	Purchase Cost Expression
T_1	$Z_{T1} = \frac{479.34 \cdot \dot{m}_5 \$\$}{0.92 - \eta_{T1}} Ln\left(\frac{P_5}{P_6}\right)(1 + \exp(0.036T_5 - 54.4))$
C_1	$Z_{C1} = \frac{71.1 \cdot \dot{m}_1}{0.9 - \eta_{C1}} \left(\frac{P_2}{P_1}\right) Ln\left(\frac{P_2}{P_1}\right)$
C_2	$Z_{C2} = \frac{71.1 \cdot \dot{m}_8}{0.9 - \eta_{C_2}} \left(\frac{P_3}{P_8}\right) Ln\left(\frac{P_3}{P_8}\right)$
HTR	$Z_{HTR} = 2681\ A_{HTR}^{0.59}$
LTR	$Z_{LTR} = 2681\ A_{LTR}^{0.59}$
Pre	$Z_{Pre} = 2681\ A_{Pre}^{0.59}$
C	$Z_{C} = \left(\frac{75 \cdot \dot{m}_{air}}{0.9 - \eta_{is,C}}\right) \left(\frac{P_{out}}{P_{in}}\right) Ln\left(\frac{P_{out}}{P_{in}}\right)$
CC	$Z_{CC} = 48.64 \cdot \dot{m}_{air(gas)} \cdot (1 + \exp(0.018T_{out} - 26.4)) \cdot \left(\frac{1}{0.995 - \frac{P_{out}}{P_{in}}}\right)$
GT	$Z_{GT} = \frac{1536 \cdot \dot{m}_{gas}}{0.92 - \eta_{is,GT}} \left(\frac{P_{out}}{P_{in}}\right)(1 + \exp(0.036T_{in} - C_{34}))$
AP	$Z_{AP} = 4122 \cdot A_{AP}^{0.59}$
gasifier	$Z_{gasifier} = 1600 \cdot \left(\dot{m}_{dry-biomass}\left[\frac{kg}{h}\right]\right)^{0.67}$

5. Results and Discussion

5.1. Parametric Assessment

In this section, a comprehensive parametric investigation is undertaken to discern the influences of key parameters, including RPs_{CO2}, $CETD_{HE2}$, $CETD_{HE3}$, and T_3. The purpose of this investigation is to elucidate the contributions of these parameters to the thermodynamic behavior of the system.

Figure 2 shows the complex interaction between RP_{GTC} and four key variables: $\dot{W}_{net}$, η_{II}, $\dot{m}_{fw}$, and SUCP. Notably, the green curve illustrating the connection between RP_{GTC} and SUCP demonstrates a gradual upward pattern from its starting point; this patter occurs because, as the value of RP_{GTC} increases, the turbine and compressor have a more complex structure, which increases the price. Interestingly, the lowest point of SUCP is seen at RP_{GTC} = 8, while the highest is reached at RP_{GTC} = 16. Simultaneously, another curve is used to show how $\dot{m}_{fw}$ behaves with changes in RP_{GTC}. At the beginning of the figure, there is a decrease until it reaches the lowest value, approximately at RP_{GTC} = 11.5. Following this, there is a subsequent increase that continues until the end. The reason for this behavior is that the gas turbine generates the largest portion of the produced net power and is the most efficient cycle. Therefore, when the efficiency is at its maximum, the gas turbine cycle absorbs most of the heat from the exhaust gas, and the power production in bottoming cycles drops. As mentioned, the RO unit only uses a portion of the bottoming cycles' produced power so the clean water production decreases as well. The changes in RP_{GTC} concerning $\dot{W}_{net}$ and η_{II} are opposite to the RP_{GTC}–$\dot{m}_{fw}$ relationship. Initially, there is a positive incline, reaching the highest values of $\dot{W}_{net}$ and η at RP_{GTC} = 11.5. After this peak, both variables start to decrease. The turbine's net work output and η_{II} increase with rising RP_{GTC}, and the turbine's net work exceeds the work consumed by the compressor. However, after the RP_{GTC} value reaches 11.5, the additional work produced in the turbine cannot exceed the additional work consumed by the compressor, resulting in a downward trend in the graph.

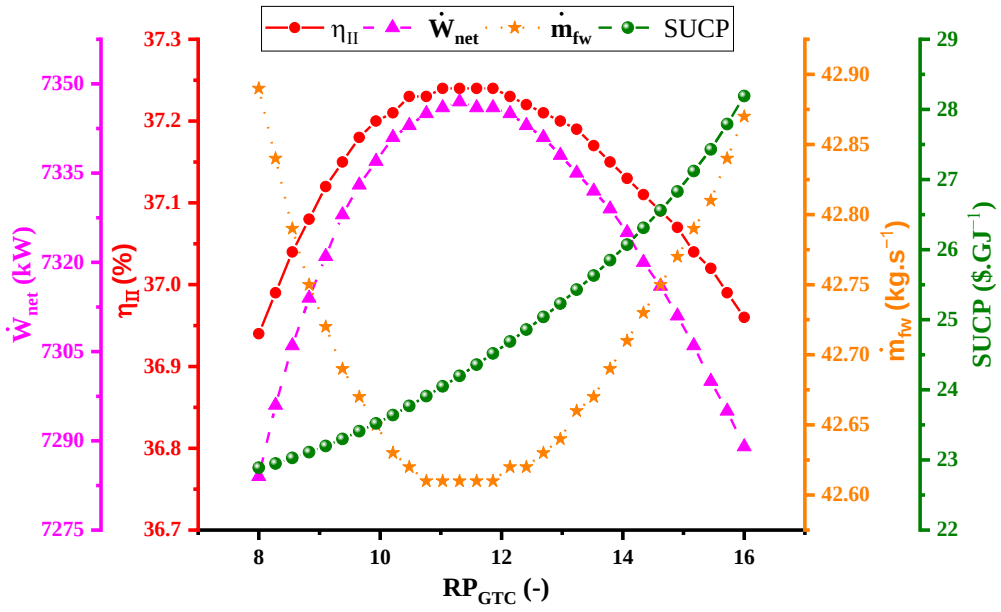

Figure 2. Relationship between RP_{GTC} and parameters $\dot{W}_{net}$, η_{II}, $\dot{m}_{fw}$, and SUCP.

Figure 3 illustrates of the relationships between RPs_{CO2} and the parameters $\dot{W}_{net}$, η_{II}, $\dot{m}_{fw}$, and SUCP. It is evident that three of these curves, RPs_{CO2}–$\dot{W}_{net}$, RPs_{CO2}–η_{II}, and RPs_{CO2}–$\dot{m}_{fw}$, exhibit a closely aligned behavior characterized by an ascent leading to a peak, where all three variables ($\dot{W}_{net}$, η_{II}, $\dot{m}_{fw}$) attain their maximum values at RP_{SCO2} = 2.23, followed by a subsequent descent. After the RPs_{CO2} value reaches its maximum, the

turbine continues to produce power, and its value is greater than the consumption in the compressor. However, after passing the maximum value, the compressor's consumption will exceed the turbine's production due to the fact that some of the production power is consumed in the reverse osmosis unit. RPs_{CO2}–$\dot{m}_{fw}$ shows a behavior similar to RPs_{CO2}–$\dot{W}_{net}$. In contrast, the fourth curve (RPs_{CO2}–SUCP) portrays a distinct trend whereby the initial increase in RP_{sCO2} results in a decrease in SUCP. However, after reaching the lowest point of SUCP at RPs_{CO2} = 1.88, the trend reverses, leading to a rise in SUCP with further RP_{sCO2} increases.

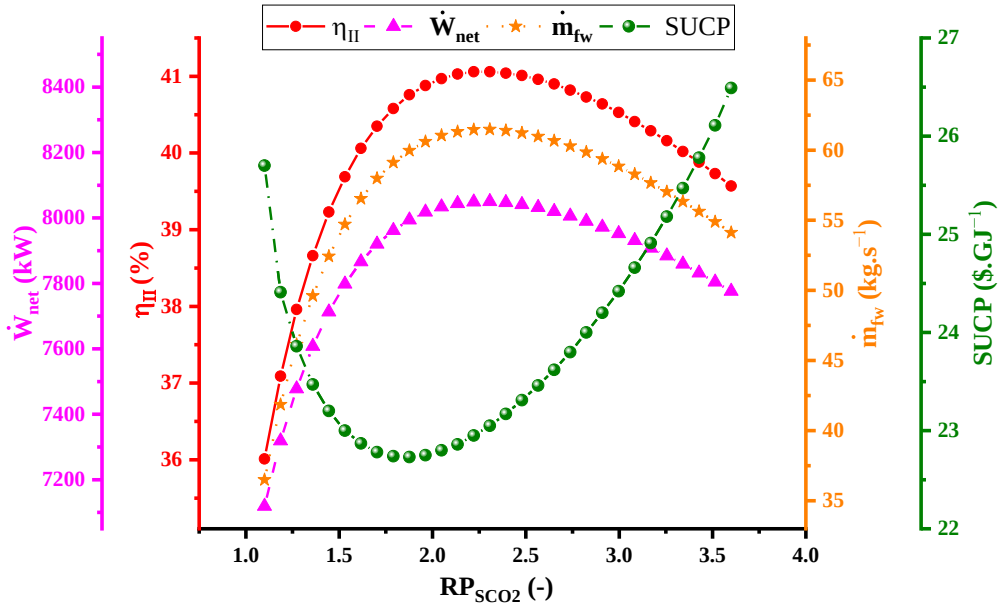

Figure 3. Relationship between RP_{SCO2} and the parameters $\dot{W}_{net}$, η_{II}, $\dot{m}_{fw}$, and SUCP.

Figure 4 presents data pertaining to the correlation between $CETD_{HE2}$ and four other variables: Wnet, η, mfw, and SUCP. These variables collectively exhibit a linear variation. Specifically, those associated with $\dot{W}_{net}$, η_{II}, $\dot{m}_{fw}$, and SUCP display positive inclines, with their lowest point observed at $CETD_{HE2}$ = 30, and the highest point at $CETD_{HE2}$ = 81. Conversely, the correlation involving SUCP exhibits a negative incline, with its minimum occurring at $CETD_{HE2}$ = 81 and its maximum at $CETD_{HE2}$ = 30. As the value of $CETD_{HE2}$ decreases, the heat transfer increases, leading to an increase in efficiency. With a rise in $CETD_{HE2}$, the heat exchanger's structural complexity which is based on its effectiveness in heat transfer decreases, and the device's cost is reduced.

Figure 5 comprises four graphs, three of which elucidate the interdependencies among $\dot{W}_{net}$, η_{II}, $\dot{m}_{fw}$, and $CETD_{HE3}$. These graphs collectively manifest a linear pattern, characterized by near-identical slopes. For a cycle with constant fuel injection, variations of the net produced power and efficiency of the system are aligned. As mentioned earlier, the production rate of clean water is proportional to the generated power. Across all three graphs, the apex is observed at $CETD_{HE3}$ = 32, while the minimum resides at $CETD_{HE3}$ = 80. Contrastingly, Figure 6, which corresponds to the variable SUCP, diverges from the preceding triad in its behavior. This curve follows a parabolic trend, and its minimum point occurs at $CETD_{HE3}$ = 58. By reducing the value of $CETD_{HE3}$, $\dot{W}_{net}$, η_{II}, and the amount of fresh water produced all decrease. Considering that, with an increase in $CETD_{HE3}$, the device is less complicated and the price also decreases. However, after it reaches the minimum value, the efficiency becomes very low, making it incompatible with cheap devices.

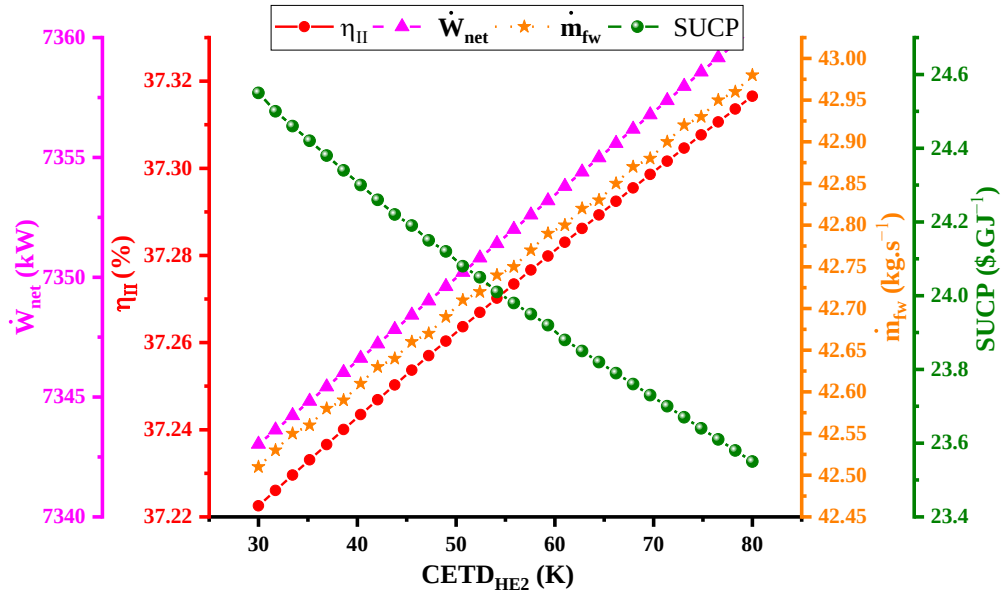

Figure 4. Relationship between $CETD_{HE2}$ and four variables: W_{net}, η, mfw, and SUCP.

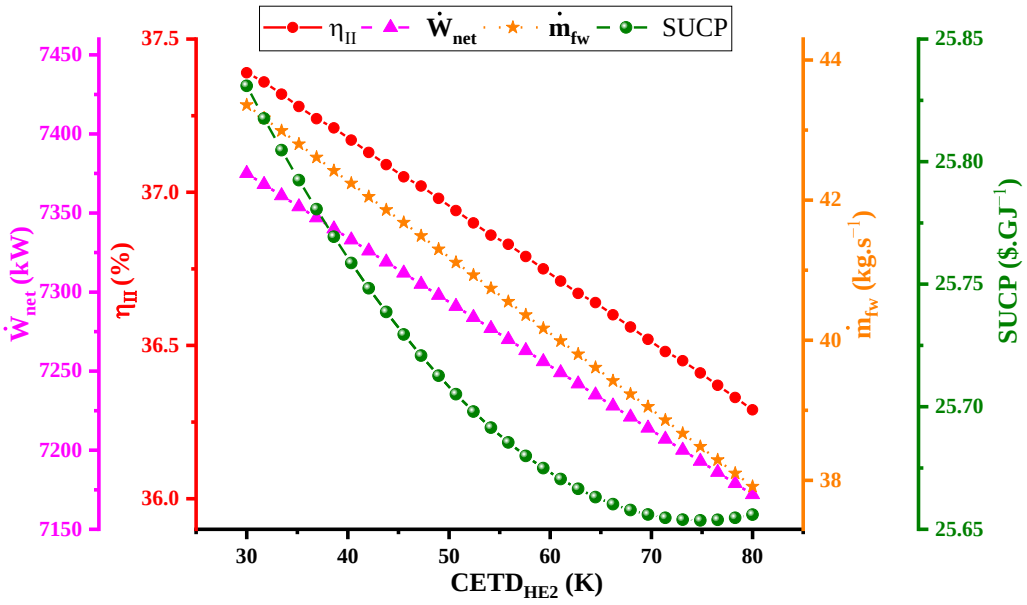

Figure 5. Relationship between $CETD_{HE3}$ and $\dot{W}_{net}$, η_{II}, and $\dot{m}_{fw}$.

Figure 6 shows the correlations among four variables, SUCP, $\dot{W}_{net}$, η_{II}, and, $\dot{m}_{fw}$, in relation to T_3 (temperature), and exhibit a diverse array of behaviors. The graph illustrating the T_3–$\dot{m}_{fw}$ relationship displays a descending trend, progressively declining as T_3 increases (based on the energy equation for HE1). Increasing the production power of the turbine decreases the thermal energy in the exhaust gases, resulting in less energy to transfer to other cycles. Considering that the electricity required by the reverse osmosis unit is supplied from the bottom cycles (sCO_2 and ORC), the rate of fresh water production decreases because the electricity production decreases. Conversely, the T_3–$\dot{W}_{net}$ and T_3–η_{II} graphs show an ascending pattern, with values steadily rising as temperature escalates. Finally, the T_3–SUCP plot demonstrates a relatively constant state initially, but upon reaching a temperature of 1500 K, it undergoes an abrupt vertical ascent. This sudden increase is a manifestation of the formula used to calculate the turbine's price; as the turbine works at a higher temperature, it is more complicated and has a higher price.

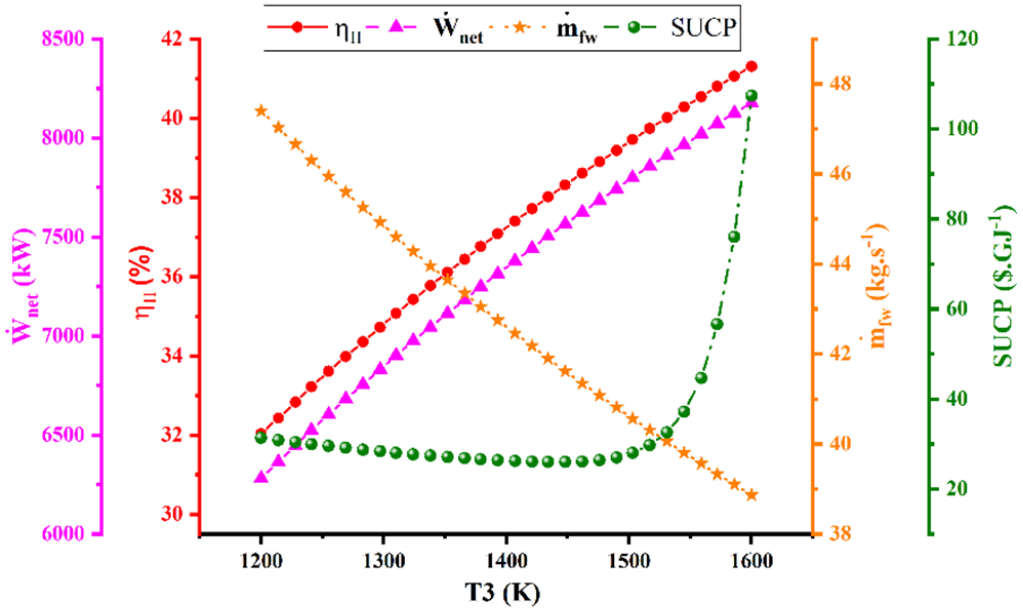

Figure 6. Relationship between T_3 and SUCP, $\dot{W}_{net}$, η_{II}, and $\dot{m}_{fw}$.

5.2. Optimization

This section focuses on the merging of machine learning principles into the domain of optimization, enriching the pursuit of optimal solutions. Within this framework, machine learning techniques analyze data to discern patterns and inform decisions. The optimization process unfolds through various stages: data collection, preprocessing, feature engineering, model training, and the application of optimization methods like the "gray wolf algorithm," alongside performance evaluation and iterative refinement. This integration facilitates data-driven decision-making processes.

In the realm of multi-objective optimization, the primary goal is to ascertain the most favorable operational configuration for a system by considering different influencing factors. Specifically, the aim is to simultaneously maximize the system's net output power and exergy efficiency while minimizing the cost of exergy per product unit and the carbon dioxide emission index. For this, a thermodynamic model of the system is crafted using EES software (V10.561), addressing equations pertaining to energy, exergy, environmental considerations, and exergy economics.

The optimization starts with the introduction of 300 random points into an artificial neural network, encompassing crucial decision-making variables as input and important performance indicators (objective functions) as output. The neural network, structured with ten layers in a feedforward configuration, effectively models the input data and predicts related output values. This training process establishes a mathematical relationship between inputs and outputs. Post-training, the resulting network, serving as a fitness function, collaborates with the gray wolf algorithm to initiate the optimization process.

The gray wolf algorithm iteratively improves and optimizes the trained model using its unique approach. The optimization endeavor employs five inputs as decision variables, detailed in Table 6. MATLAB software (R2022a) serves as the computational tool for machine learning and multi-objective optimization employing the gray wolf algorithm in this study. Fine-tuning efforts are undertaken to achieve optimal values. Two distinct optimization scenarios are considered: the first scenario comprises the pollution index, total exergy unit cost of products, and exergy efficiency as objective functions, while the second scenario includes the pollution index, total exergy unit cost of products, and net output power as objective functions [38].

Table 6. Lower and upper bounds of decision variables used in the optimization.

Decision Parameter	Lower Bound	Upper Bound
Gas turbine inlet temperature (K)	1200	1600
Air compressor pressure ratio	8	16
Cold and temperature difference of heat exchanger 2 (K)	30	80
Cold and temperature difference of heat exchanger 3 (K)	30	80

Results of Multi-Objective Optimization Using the Gray Wolf Algorithm

Utilizing the grey wolf algorithm, two distinct multi-objective optimization analyses were conducted, each employing a variety of objective functions such as environmental index ζ (kg/kWh), net output power (kW), exergy efficiency, and cost of product c_p (USD/GJ). The outcomes of these optimizations for the first and second model optimization are depicted in Figure 7a,b.

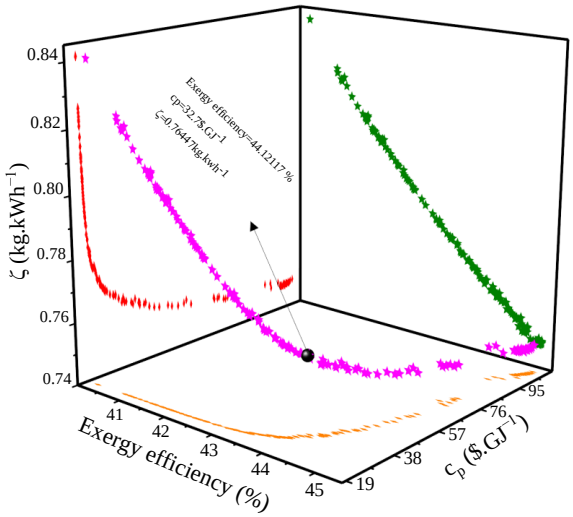

(**a**)

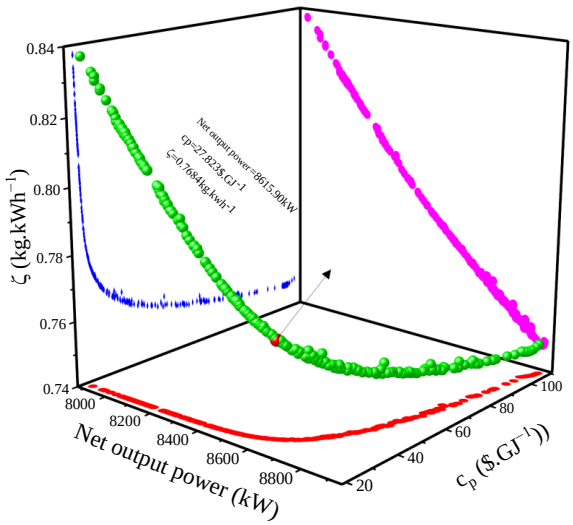

(**b**)

Figure 7. (**a**) Pareto frontier for the first model multi-objective optimization. (**b**) Pareto frontier for the second model multi-objective optimization. The application of genetic algorithms to multi-objective

optimization produced Pareto frontiers for both scenarios, as illustrated in (**a**,**b**). The proposed optimal values, taking into account three variables—ζ, cp, and exergy efficiency—are 0.7644 kg/kWh, 32.7 USD/GJ, and 44.12%, respectively. Moving to the second scenario, considering three variables—ζ, cp, and net output power—the values stand at 0.7684 kg/kWh, 27.823 USD/GJ, and 2615.90 kW, respectively.

From the initial optimization process, Figure 8a–e illustrate the scattered distribution of decision variables (RP_{SCO2}, $CETD_{HE2}$, $CETD_{HE3}$, T_3, and RP_{GTC}) within the optimal operational range. As the optimization purpose, this figure shows that the optimal values for decision variables, including RP_{SCO2}, $CETD_{HE2}$, $CETD_{HE3}$, T_3, and RP_{GTC}, fall within the ranges of 1.8–2.8, 30–40 K, 50–30 K, 1450–1600 K, and 15–9, respectively.

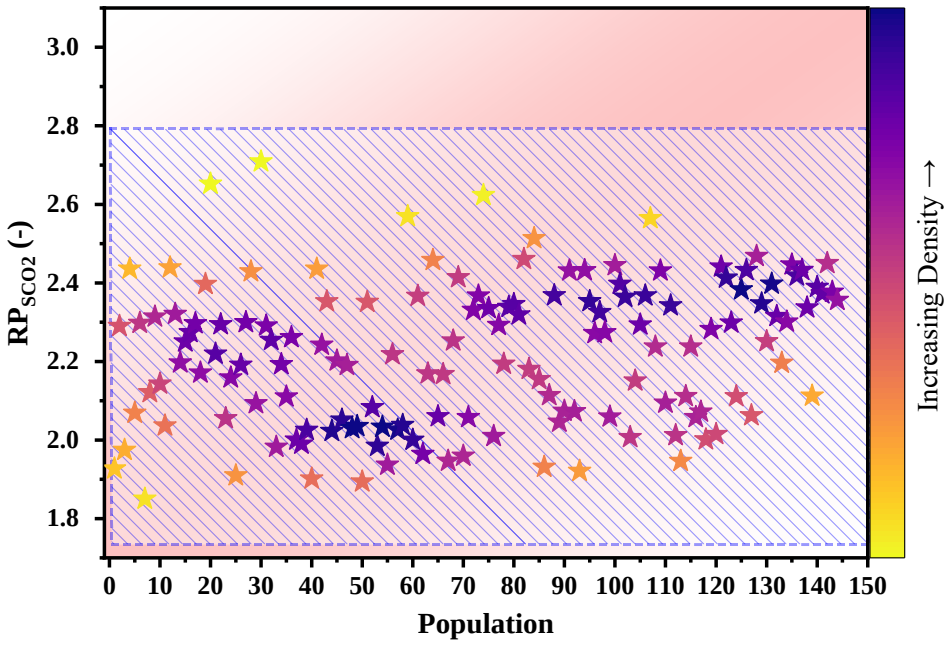

(**a**)

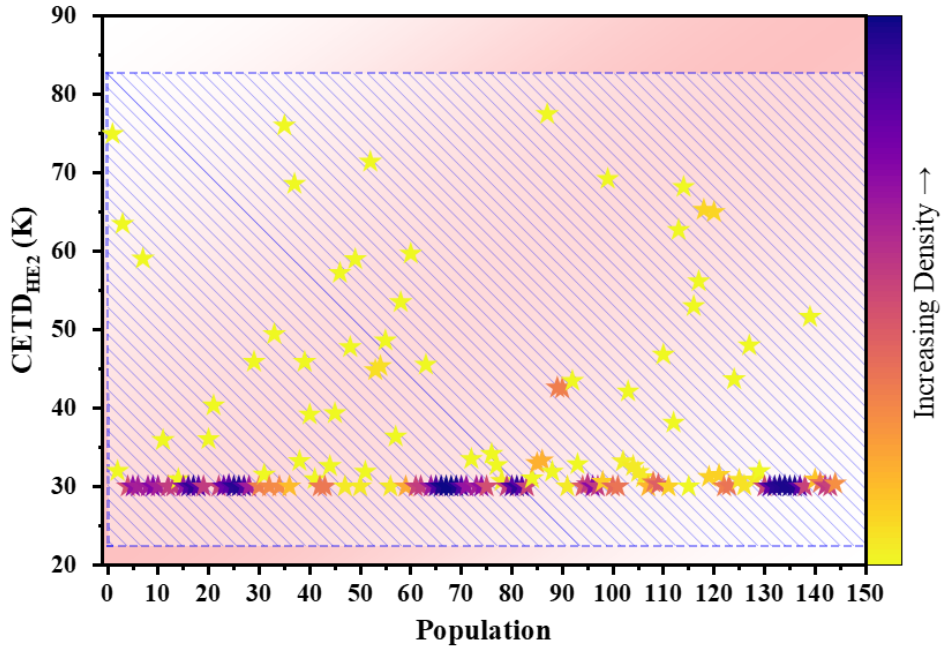

(**b**)

Figure 8. *Cont.*

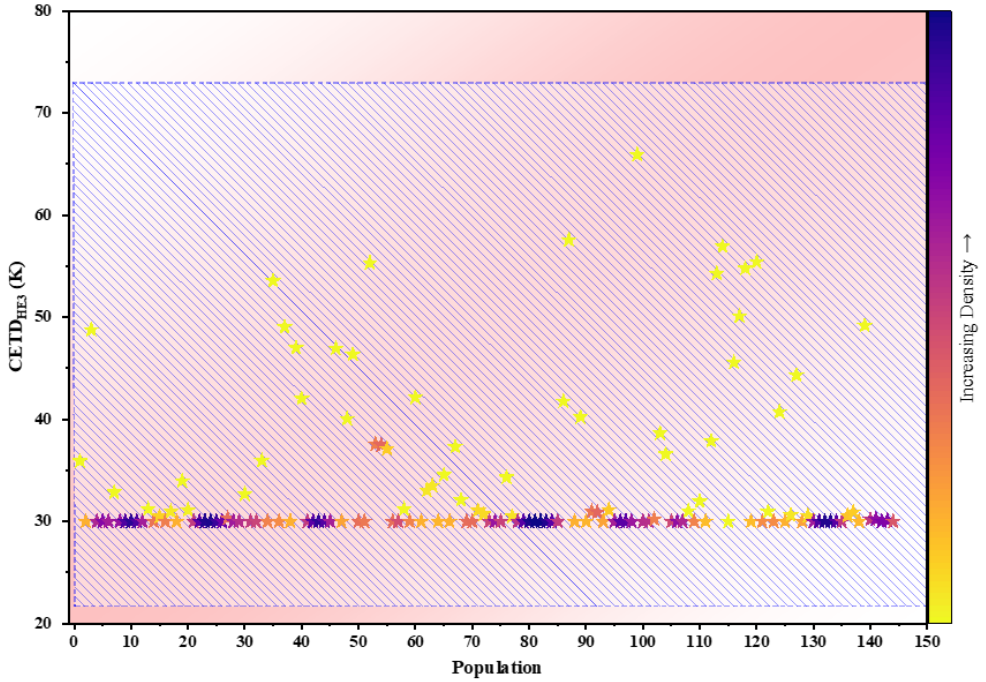

(**c**)

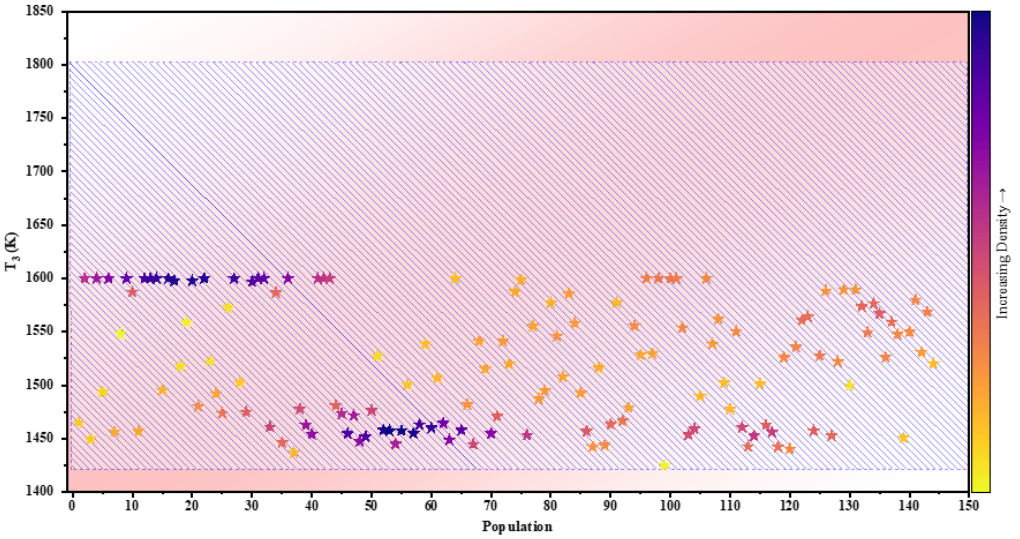

(**d**)

Figure 8. *Cont*.

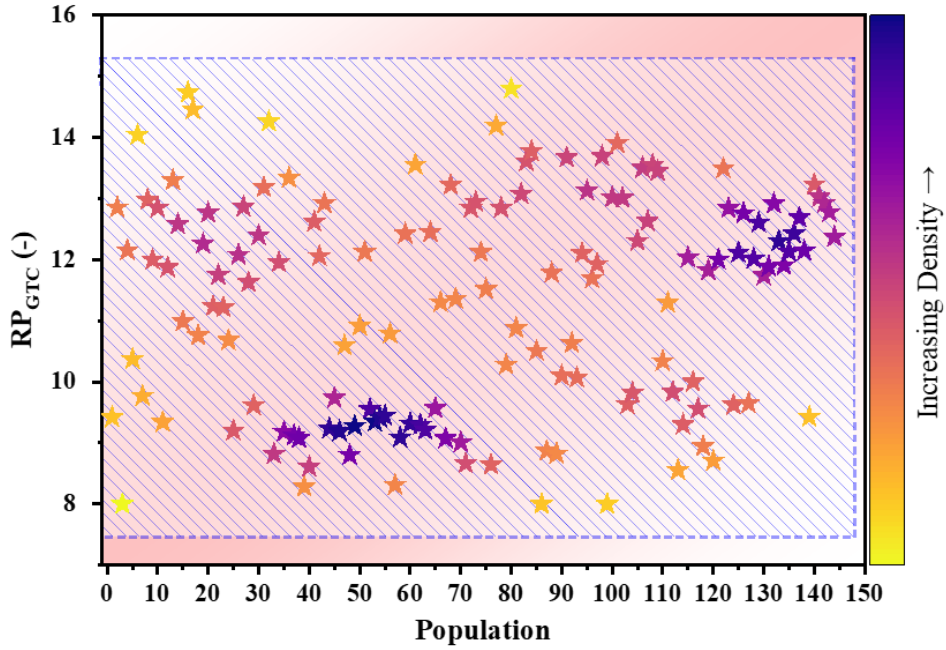

(**e**)

Figure 8. (**a**) Scattered distribution for RP_{SCO2}. (**b**) Scattered distribution for $CETD_{HE2}$. (**c**) Scattered distribution for $CETD_{HE3}$. (**d**) Scattered distribution for T_3. (**e**) Scattered distribution for RP_{GTC}.

6. Conclusions

The present study assesses a novel system for the simultaneous production of electric power and fresh water, comprising gas turbine subsystems with gasification processes, Brayton recondensation utilizing a supercritical carbon dioxide working fluid, organic Rankine cycle, and reverse osmosis. This system is assessed from energy, exergy, thermoeconomic, and environmental perspectives, and two distinct multi-objective optimization scenarios are applied featuring various objective functions. This simultaneous production system entails three power-producing subsystems and one fresh water-producing subsystem. Here, we outline the key findings derived from the study and the conclusions drawn from them:

1. At the design point, the system has an exergy efficiency of 37.24%, a carbon dioxide emission index of 0.8977 kg/kWh, a unit cost of exergy products of 24.31 USD/GJ, a mass flow rate of produced fresh water of 42/61 kg/s, a total exergy destruction rate of 11,398 kW, and a net power production of 7347 kW.
2. The parametric study shows that increasing the gas turbine pressure ratio results in escalating total unit cost of exergy products, net output power, and exergy efficiency initially, followed by a subsequent decline, while the mass flow rate of fresh water produced exhibits an opposite trend.
3. Altering the pressure ratio of the Brayton recondensation subsystem utilizing supercritical carbon dioxide working fluid initially enhanced net output power, fresh water mass flow rate, and exergy efficiency before undergoing a decrease, while the unit cost of exergy products displays an initial reduction followed by an increase.
4. Elevating the temperature difference of the cold terminal of heat exchanger 2 from 30 K to 80 K leads to linear increases in exergy efficiency, net power output, and fresh water mass flow, coupled with a linear decrease in the cost of exergy unit of products.
5. Increasing the temperature difference of the cold terminal of heat exchanger 3 leads to a reduction in exergy efficiency, net output power, and mass flow rate of fresh water production, with the unit cost of exergy products exhibiting an initial decline followed by a rise.

6. Gas turbine inlet temperature exhibits a direct relationship with exergy efficiency and net output power, and an inverse correlation with the mass flow rate of fresh water produced. Furthermore, raising the inlet temperature of the gas turbine from 1200 K to 1600 K initially leads to a decrease followed by a rise in the unit cost of exergy products of the system.
7. In the first optimization scenario, considering the pollution index, total unit cost of exergy products, and exergy efficiency as objective functions, the optimal values are, respectively, identified as 0.7644 kg/kWh, 32.7 USD/GJ, and 44%. Conversely, in the second optimization scenario, featuring the emission index, total unit cost of exergy products, and output net power as objective functions, optimal values are 0.7684 kg/kWh, 27.82 USD/GJ, and 2615.9 kW.

Based on the findings, further research appears to be merited on this topic, including life cycle analysis for better environmental assessments and advanced exergy and exergoeconomic analyses for better thermodynamic and economic understanding.

Author Contributions: Conceptualization, F.P.G., N.G., S.S. and M.A.R.; Methodology, F.P.G., S.S.L., S.S. and M.A.R.; Software, F.P.G., S.S.L., N.G., S.S. and M.A.R.; Validation, F.P.G., S.S.L., N.G., S.S. and M.A.R.; Formal analysis, F.P.G., S.S.L., N.G., S.S. and M.A.R.; Investigation, F.P.G., S.S.L., N.G., S.S. and M.A.R.; Resources, F.P.G., S.S.L., N.G., S.S. and M.A.R.; Data curation, Saeed Soltani; Writing—original draft, F.P.G., S.S.L., N.G., S.S. and M.A.R.; Visualization, Saeed Soltani; Supervision, S.S. and M.A.R. All authors have read and agreed to the published version of the manuscript.

Funding: This research received no external funding.

Data Availability Statement: No new data were created or analyzed in this study.

Conflicts of Interest: The authors declare no conflict of interest.

Abbreviations

AC	Air compressor
BPu	Boost pump
c	Cost per exergy unit, USD/GJ
$c_{p,tot}$	Total product unit cost, USD/GJ
C	Compressor
CC	Combustion chamber
Cond	Condenser
CRF	Capital recovery factor
$\dot{C}$	Cost rate, USD/h
$\dot{E}$	Exergy rate, kW
FPu	Feed pump
f_k	Exergoeconomic factor
GT	Gas turbine
GTIT	Gas turbine inlet temperature, K
h	Specific enthalpy, kJ/kg
HE	Heat exchanger
HPPu	High-pressure pump
HTR	High-temperature recuperator
IPCC	Intergovernmental Panel on Climate Change
K	Equilibrium constant
LHV	Higher heating value, kJ/kg
LTR	Low temperature recuperator
$\dot{m}$	Mass flow rate, kg/s
ORC	Organic Rankine cycle
P	Pressure, kPa
PT	Pelton turbine
$\dot{Q}$	Heat rate, MW

REC	Recompression compressor
Reg	Regenerator
RES	Renewable energy sources
RO	Reverse osmosis
r_p	Pressure ratio
r_k	Relative cost difference
sCO_2	Supercritical carbon dioxide
ST	Steam turbine
ST_{ORC}	Series of two-stage organic Rankine cycles
T	Temperature, K
T_g	Gasifier's temperature, K
$\dot{W}$	Work rate done/absorbed, MW
y_s	Salt water mass fraction
$\dot{Z}$	Purchased equipment cost, USD/h
η_{is}	Isentropic efficiency
ζ	Carbon dioxide emission index
ε	Effectiveness
$\varnothing_r$	Maintenance factor
CI	*Capital investment*
OM	*Repair and maintenance*
g	Gasifier
is	Isentropic
in	Inlet
out	Outlet
D	Destroyed
1, 2, . . . 42	Numbers of states

References

1. Wang, L.; Wang, L.; Li, Y.; Wang, J. A century-long analysis of global warming and earth temperature using a random walk with drift approach. *Decis. Anal. J.* **2023**, *7*, 100237. [CrossRef]
2. Akan, T. Can renewable energy mitigate the impacts of inflation and policy interest on climate change? *Renew. Energy* **2023**, *214*, 255–289. [CrossRef]
3. Esily, R.R.; Yuanying, C.; Ibrahiem, D.M.; Houssam, N.; Makled, R.A.; Chen, Y. Environmental benefits of energy poverty alleviation, renewable resources, and urbanization in North Africa. *Util. Policy* **2023**, *82*, 101561. [CrossRef]
4. Senegačnik, A.; Stropnik, R.; Sekavčnik, M.; Oprešnik, S.R.; Mlakar, U.; Ivanjko, Š.; Stritih, U. Integration of renewable energy sources for sustainable energy development in Slovenia till 2050. *Sustain. Cities Soc.* **2023**, *96*, 104668. [CrossRef]
5. Gul, E.; Baldinelli, G.; Bartocci, P.; Shamim, T.; Domenighini, P.; Cotana, F.; Wang, J.; Fantozzi, F.; Bianchi, F. Transition toward net zero emissions—Integration and optimization of renewable energy sources: Solar, hydro, and biomass with the local grid station in central Italy. *Renew. Energy* **2023**, *207*, 672–686. [CrossRef]
6. Ioannidis, F.; Kosmidou, K.; Papanastasiou, D. Public awareness of renewable energy sources and Circular Economy in Greece. *Renew. Energy* **2023**, *206*, 1086–1096. [CrossRef]
7. Algarni, S.; Tirth, V.; Alqahtani, T.; Alshehery, S.; Kshirsagar, P. Contribution of renewable energy sources to the environmental impacts and economic benefits for sustainable development. *Sustain. Energy Technol. Assess.* **2023**, *56*, 103098. [CrossRef]
8. Kocak, E.; Ulug, E.E.; Oralhan, B. The impact of electricity from renewable and non-renewable sources on energy poverty and greenhouse gas emissions (GHGs): Empirical evidence and policy implications. *Energy* **2023**, *272*, 127125. [CrossRef]
9. Zabat, L.H.; Akli Sadaoui, N.; Abid, M.; Sekrafi, H. Threshold effects of renewable energy consumption by source in U.S. economy. *Electr. Power Syst. Res.* **2022**, *213*, 108669. [CrossRef]
10. Fakudze, S.; Chen, J. A critical review on co-hydrothermal carbonization of biomass and fossil-based feedstocks for cleaner solid fuel production: Synergistic effects and environmental benefits. *Chem. Eng. J.* **2023**, *457*, 141004. [CrossRef]
11. Verma, S.; Dregulo, A.M.; Kumar, V.; Bhargava, P.C.; Khan, N.; Singh, A.; Sun, X.; Sindhu, R.; Binod, P.; Zhang, Z.; et al. Reaction engineering during biomass gasification and conversion to energy. *Energy* **2023**, *266*, 126458. [CrossRef]
12. Wang, J.; Fu, J.; Zhao, Z.; Bing, L.; Xi, F.; Wang, F.; Dong, J.; Wang, S.; Lin, G.; Yin, Y.; et al. Benefit analysis of multi-approach biomass energy utilization toward carbon neutrality. *Innovation* **2023**, *4*, 100423. [CrossRef] [PubMed]
13. Ghorbani, S.; Atashkari, K.; Borji, M. Three-stage model-based evaluation of a downdraft biomass gasifier. *Renew. Energy* **2022**, *194*, 734–745. [CrossRef]

14. Drobniak, A.; Jelonek, Z.; Mastalerz, M.; Jelonek, I. Residential gasification of solid biomass: Influence of raw material on emissions. *Int. J. Coal Geol.* **2023**, *271*, 104247. [CrossRef]
15. Ngamsidhiphongsa, N.; Limleamthong, P.; Chalermsinsuwan, B.; Prasertcharoensuk, P.; Wiyaratn, W.; Arpornwichanop, A. Application of computational fluid dynamics and response surface methodology in downdraft gasification using multiple biomass pellets. *J. Clean. Prod.* **2023**, *417*, 137923. [CrossRef]
16. Batista, N.E.; Carvalho, P.C.M.; Fernández-Ramírez, L.M.; Braga, A.P.S. Optimizing methodologies of hybrid renewable energy systems powered reverse osmosis plants. *Renew. Sustain. Energy Rev.* **2023**, *182*, 113377. [CrossRef]
17. Zubair, M.M.; Saleem, H.; Zaidi, S.J. Recent progress in reverse osmosis modeling: An overview. *Desalination* **2023**, *564*, 116705. [CrossRef]
18. Kolathur, S.; Khatiwada, D.; Khan, E.U. Life cycle assessment and life cycle costing of a building-scale, solar-driven water purification system. *Energy Nexus* **2023**, *10*, 100208. [CrossRef]
19. Alawad, S.M.; Mansour, R.B.; Al-Sulaiman, F.A.; Rehman, S. Renewable energy systems for water desalination applications: A comprehensive review. *Energy Convers. Manag.* **2023**, *286*, 117035. [CrossRef]
20. Javaherian, A.; Yari, M.; Gholamian, E.; Carton, J.G.; Mehr, A.S. Proposal and comprehensive analysis of power and green hydrogen production using a novel integration of flame-assisted fuel cell system and Vanadium-Chlorine cycle: An application of multi-objective optimization. *Energy Convers. Manag.* **2023**, *277*, 116659. [CrossRef]
21. Ahmad, A.A.; Zawawi, N.A.; Kasim, F.H.; Inayat, A.; Khasri, A. Assessing the gasification performance of biomass: A review on biomass gasification process conditions, optimization and economic evaluation. *Renew. Sustain. Energy Rev.* **2016**, *53*, 1333–1347. [CrossRef]
22. Li, Y.; Zhang, L.; Zhao, W.; Song, X.; Wei, J.; Bai, Y.; Wang, J.; Yu, G. Biomass erosion and its effect on heat carrying performance of alumina heat carrier during multiple cycle sintering in solar photothermal coupled with biomass gasification. *Chem. Eng. Sci.* **2024**, 120807. [CrossRef]
23. Yilmaz, F.; Ozturk, M.; Selbas, R. Design and thermodynamic assessment of a biomass gasification plant integrated with Brayton cycle and solid oxide steam electrolyzer for compressed hydrogen production. *Int. J. Hydrog. Energy* **2020**, *45*, 34620–34636. [CrossRef]
24. Chen, H.; Lu, D.; An, J.; Qiao, S.; Dong, Y.; Jiang, X.; Xu, G.; Liu, T. Thermo-Economic analysis of a novel biomass Gasification-Based power system integrated with a supercritical CO_2 cycle and a Coal-Fired power plant. *Energy Convers. Manag.* **2022**, *266*, 115860. [CrossRef]
25. Roy, D. Multi-objective optimization of biomass gasification based combined heat and power system employing molten carbonate fuel cell and externally fired gas turbine. *Appl. Energy* **2023**, *348*, 121486. [CrossRef]
26. Blanco-Marigorta, A.M.; Masi, M.; Manfrida, G. Exergo-environmental analysis of a reverse osmosis desalination plant in Gran Canaria. *Energy* **2014**, *76*, 223–232. [CrossRef]
27. Abbasi, H.R.; Pourrahmani, H. Multi-objective optimization and exergoeconomic analysis of a continuous solar-driven system with PCM for power, cooling and freshwater production. *Energy Convers. Manag.* **2020**, *211*, 112761. [CrossRef]
28. Nemati, A.; Sadeghi, M.; Yari, M. Exergoeconomic analysis and multi-objective optimization of a marine engine waste heat driven RO desalination system integrated with an organic Rankine cycle using zeotropic working fluid. *Desalination* **2017**, *422*, 113–123. [CrossRef]
29. Abdolalipouradl, M.; Mohammadkhani, F.; Khalilarya, S.; Yari, M. Thermodynamic and exergoeconomic analysis of two novel tri-generation cycles for power, hydrogen and freshwater production from geothermal energy. *Energy Convers. Manag.* **2020**, *226*, 113544. [CrossRef]
30. Pan, M.; Zhu, Y.; Bian, X.; Liang, Y.; Lu, F.; Ban, Z. Theoretical analysis and comparison on supercritical CO_2 based combined cycles for waste heat recovery of engine. *Energy Convers. Manag.* **2020**, *219*, 113049. [CrossRef]
31. Song, J.; Wang, Y.; Wang, K.; Wang, J.; Markides, C.N. Combined supercritical CO_2 (SCO_2) cycle and organic Rankine cycle (ORC) system for hybrid solar and geothermal power generation: Thermoeconomic assessment of various configurations. *Renew. Energy* **2021**, *174*, 1020–1035. [CrossRef]
32. Khoshgoftar Manesh, M.H.; Firouzi, P.; Kabiri, S.; Blanco-Marigorta, A.M. Evaluation of power and freshwater production based on integrated gas turbine, S-CO_2, and ORC cycles with RO desalination unit. *Energy Convers. Manag.* **2021**, *228*, 113607. [CrossRef]
33. Wang, S.; Liu, C.; Li, J.; Sun, Z.; Chen, X.; Wang, X. Exergoeconomic analysis of a novel trigeneration system containing supercritical CO2 Brayton cycle, organic Rankine cycle and absorption refrigeration cycle for gas turbine waste heat recovery. *Energy Convers. Manag.* **2020**, *221*, 113064. [CrossRef]
34. Soltani, S.; Mahmoudi, S.M.S.; Yari, M.; Rosen, M.A. Thermodynamic analyses of a biomass integrated fired combined cycle. *Appl. Therm. Eng.* **2013**, *59*, 60–68. [CrossRef]
35. Zainal, Z.A.; Ali, R.; Lean, C.H.; Seetharamu, K.N. Prediction of performance of a downdraft gasifier using equilibrium modeling for different biomass materials. *Energy Convers. Manag.* **2001**, *42*, 1499–1515. [CrossRef]
36. Bejan, A.; Tsatsaronis, G.; Moran, M.J. *Thermal Design and Optimization*; Wiley: Wiley-Interscience Publication: Hoboken, NJ, USA, 1995; ISBN 9780471584674.

37. Moharramian, A.; Soltani, S.; Rosen, M.A.; Mahmoudi, S.M.S.; Jafari, M. Conventional and enhanced thermodynamic and exergoeconomic analyses of a photovoltaic combined cycle with biomass post firing and hydrogen production. *Appl. Therm. Eng.* **2019**, *160*, 113996. [CrossRef]
38. Javaherian, A.; Ghasemzadeh, N.; Javanshir, N.; Yari, M.; Vajdi, M.; Nami, H. Techno-environmental assessment and machine learning-based optimization of a novel dual-source multi-generation energy system. *Process Saf. Environ. Prot.* **2023**, *176*, 537–559. [CrossRef]